AIAA 91-3209

Generic Hypersonic Inlet Module Analysis

Charles E. Cockrell, Jr.
Lawrence D. Huebner
NASA-Langley Research Center
Hampton, VA

AIAA 9th
Applied Aerodynamics Conference
September 24-26, 1991 / Baltimore, MD

GENERIC HYPERSONIC INLET MODULE ANALYSIS

Charles E. Cockrell, Jr.*
Lawrence D. Huebner †
NASA Langley Research Center
Hampton, VA

Abstract

A computational study associated with an internal inlet drag analysis was performed for a generic hypersonic inlet module. The purpose of this study was to determine the feasibility of computing the internal drag force for a generic scramjet engine module using computational methods. The computational study consisted of obtaining two-dimensional (2D) and three-dimensional (3D) computational fluid dynamics (CFD) solutions using the Euler and parabolized Navier-Stokes (PNS) equations. The solution accuracy was assessed by comparisons with experimental pitot pressure data. The CFD analysis indicates that the 3D PNS solutions show the best agreement with experimental pitot pressure data. The internal inlet drag analysis consisted of obtaining drag force predictions based on experimental data and 3D CFD solutions. A comparative assessment of each of the drag prediction methods is made and the sensitivity of CFD drag values to computational procedures is documented. The analysis indicates that the CFD drag predictions are highly sensitive to the computational procedure used.

Nomenclature

dA,ΔA= differential area for drag force computation, ft^2
F_I = $-R_x$ = internal drag force on inlet, lbf
I,J,K = grid point indices
L_1 = distance from wall to first cell center, ft.
$\dot{m}$ = mass flow rate, lbm/ft^3
M = local Mach number
P = static pressure, lbf/in^2
P_o = stagnation pressure, lbf/in^2
P_p = pitot pressure, lbf/in^2
R = universal gas constant, 1716 $ft^2/(^oR\text{-}sec^2)$
R_x = Shear force on control volume, lbf
T = Static temperature, ^oF
T_o = stagnation temperature, ^oF
U_1 = velocity at first cell center next to wall, ft/sec
u = local streamwise component of velocity, ft/sec
V = local velocity, ft/sec
y^+ = inner law variable (see equation 1)
ΔX,ΔY = dimensions of differential area for drag force computation, ft
γ = specific heat ratio, C_p/C_v
μ = viscosity coefficient, lbm/(ft-sec)
ρ = density, lbm/ft^2

Subscripts

1 = conditions at first cell center away from wall, (See equation 1)

I. Introduction

The recent attention in generic hypersonics research is driven by an interest in hypersonic, air-breathing aircraft, such as the National Aero-Space Plane (NASP). The use of air-breathing propulsion provides for significant performance advantages over rocket propulsion systems for the mission requirements of NASP-like vehicles[1]. Body-mounted, supersonic combustion ramjet (SCRAMJET) engines are prime candidates for hypersonic, air-breathing propulsion. A design characteristic of such a vehicle is that the propulsion system must be highly integrated with the airframe. The forebody surface of the vehicle provides compression of the flow before reaching the inlet, and the aftbody surface serves as an extension of the nozzle to expand the flow and provide for maximum thrust[2]. Additionally, the engine modules are mounted inside the vehicle's bow shock wave, which provides for a significant size and weight savings for the propulsion system[3]. The boundary layer that forms on the forebody surface is swallowed by the inlet. Due to these design features, there are a number of issues that must be addressed in the area of propulsion/airframe integration for this class of vehicle. One such issue is force accounting for wind tunnel models used in powered testing to simulate scramjet exhaust flows. Specifically, it is necessary to account for the external forces and moments when testing individual metric components of these models, such as the forebody and powered aftbody. The total forces on the forebody/inlet region from the nose to the cowl trailing edge may be measured by examining a generic forebody/inlet model with a flow-through inlet configuration. In order to obtain an accurate accounting of the external force on

* Aerospace Engineer, Supersonic/Hypersonics Aerodynamics Branch, Applied Aerodynamics Division, Member AIAA.
†Aerospace Engineer, Hypersonics Group Leader, Supersonic/Hypersonics Aerodynamics Branch, Applied Aerodynamics Division, Member AIAA.

the forebody/inlet region, an accurate estimation of the internal inlet drag force must be obtained, so it may be subtracted from the balance reading. The estimation of internal drag force may be performed using experimental or computational methods.

It is anticipated that CFD will be heavily utilized in the design process for a hypersonic, air-breathing vehicle. The ground test facilities currently available are unable to represent all aspects of the full-scale configuration at the flight conditions associated with this class of vehicle[2]. Efforts are underway to validate CFD codes and establish criteria for credible CFD results[4]. It is desirable to account for the internal force on the inlet region of the engine using CFD flow-field solutions, due to the difficulty of determining this value using experimental methods. Therefore, the feasibility of using computational tools to perform this estimation must be assessed.

The major objectives of the study presented herein were twofold. The first objective was to perform a computational analysis of a single inlet module for a generic, body-mounted scramjet propulsion system. The analysis consisted of obtaining 2D and 3D CFD solutions using the Euler and parabolized Navier-Stokes (PNS) equations. Solution accuracy was assessed by comparisons with experimental pitot pressure data. The second objective was to perform an internal inlet drag analysis in which predictions for internal drag force are made using the 3D CFD solutions and experimental data. A comparative assessment is made of each approach and the sensitivity of CFD drag predictions to various computational methods (such as grid size, boundary conditions, and other input parameters) is documented. Secondary objectives of the study were to provide further validation for a recently released CFD code and to provide documentation relating to the computation of this class of hypersonic flow field.

This paper presents a description of the forebody/inlet model tested and the experimental data previously obtained. The computational procedure and selected CFD solutions are presented. Comparisons of the experimental and computational data are also presented together with comparisons of various CFD solutions to show the effects of CFD input parameters on solution accuracy. The method of computing the internal drag force is described and computational drag force predictions are given.

II. Model Description

The investigation was conducted on the inlet of a generic forebody/inlet model for a body-mounted scramjet propulsion system. The flow-field features represented here are typical of those seen in designs for scramjet engines. It is appropriate to investigate the forebody/inlet region of the engine separately because the flow is independent of the nozzle and aftbody regions[3]. Experimental data, obtained previously from a wind tunnel test of this model, were used to assess the accuracy of CFD solutions and to compute the internal drag force.

A diagram of the inlet is shown in Figure 1. The bottom view shows two inlet modules mounted on the underside of the model. Due to symmetry, the analysis was conducted for only a single module as shown by the shaded portion of the bottom and oblique views in Figure 1. The two modules are separated by a strut which causes a compression of the flow just past the inflow

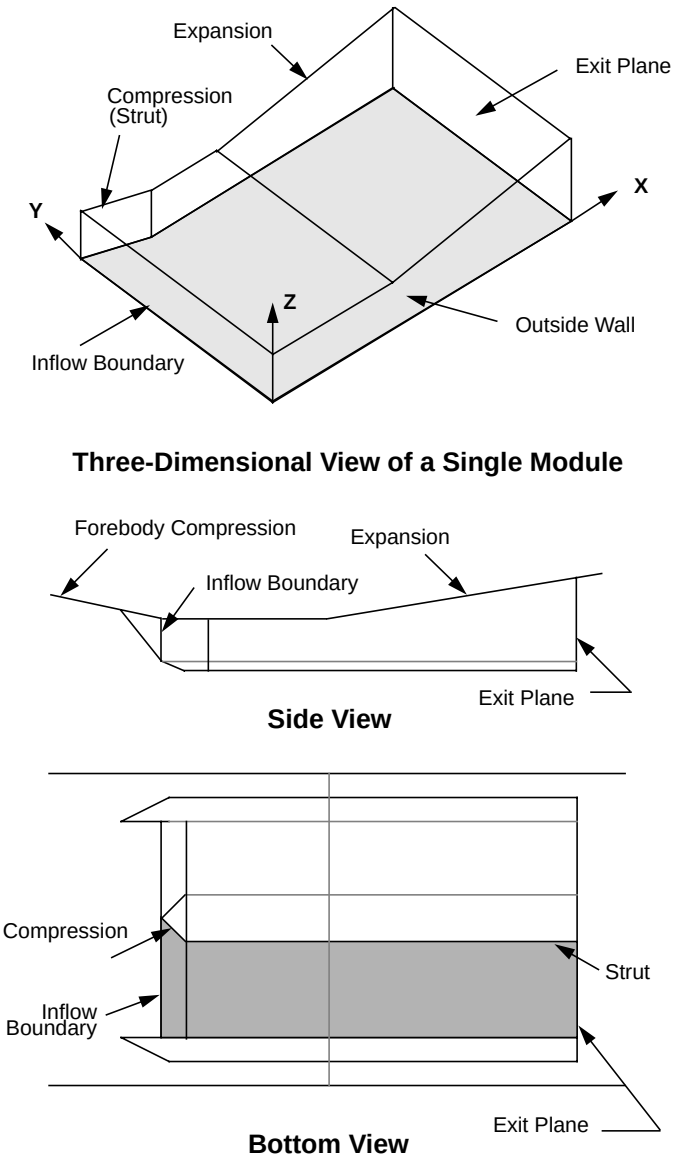

Figure 1
Diagram of Hypersonic Inlet Module

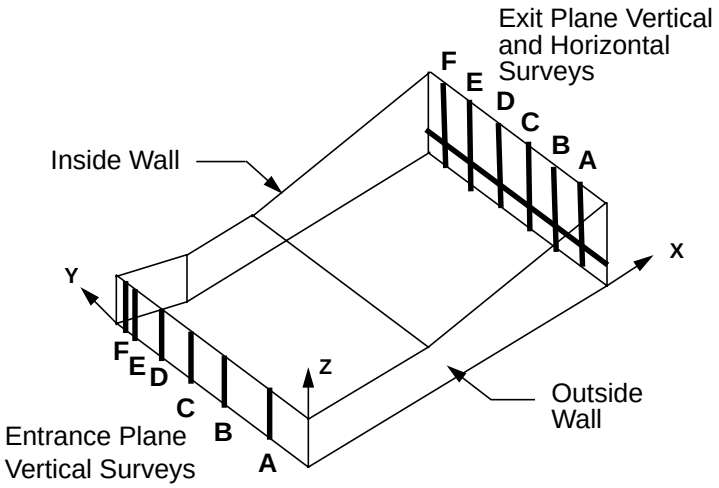

Entrance Plane Vertical Survey Locations

STATION	DIST. FROM OUTSIDE WALL (IN.)
A	0.318
B	0.949
C	1.582
D	2.215
E	2.632
F	2.782

Exit Plane Vertical Survey Locations

STATION	DIST. FROM OUTSIDE WALL (IN.)
A	0.100
B	0.492
C	1.077
D	1.662
E	2.247
F	2.638

Exit Plane Horizontal Survey Location

0.215 inches from lower surface

Figure 2
Locations of Experimental Pressure Surveys

boundary inside the inlet module. The side view shows other geometry features represented in this configuration. Compression of the flow takes place along the forebody surface and the forebody boundary layer is swallowed by the inlet. An expansion takes place inside the inlet module along its upper surface. The oblique view in the figure also shows the orientation of the coordinate axes system.

Experimental pressure surveys were taken at the entrance and exit planes of the inlet module. The survey locations are shown in Figure 2. The test was conducted at freestream conditions of Mach 6.0, a total pressure of 100 psia, and a Reynolds number of approximately 2.0 x 10^6 per foot. Vertical surveys of static and pitot pressures were taken at the entrance and exit planes as well as one horizontal survey of pitot pressures at the exit plane. Samples of experimental pitot pressure surveys are shown in Figure 3. Figure 3(a) shows a vertical

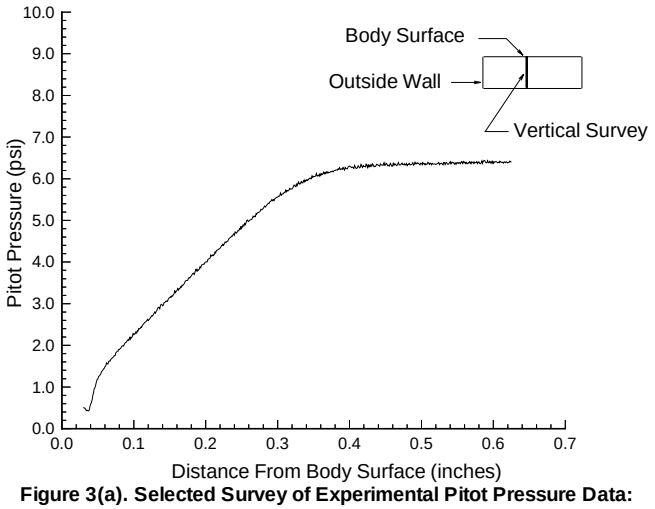

Figure 3(a). Selected Survey of Experimental Pitot Pressure Data: Entrance Plane Vertical Survey at Station C

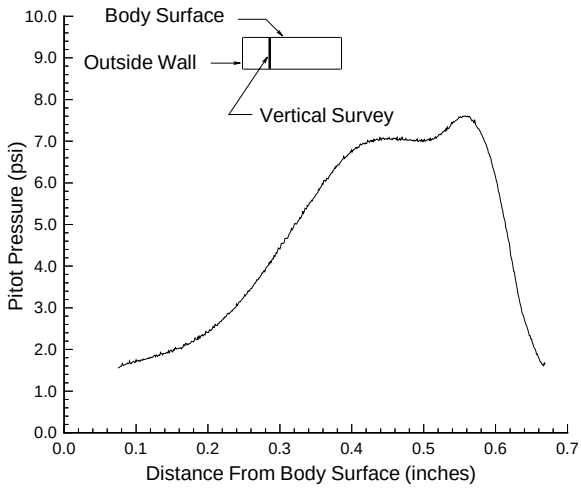

Figure 3(b). Selected Survey of Experimental Pitot Pressure Data: Exit Plane Vertical Survey at Station C

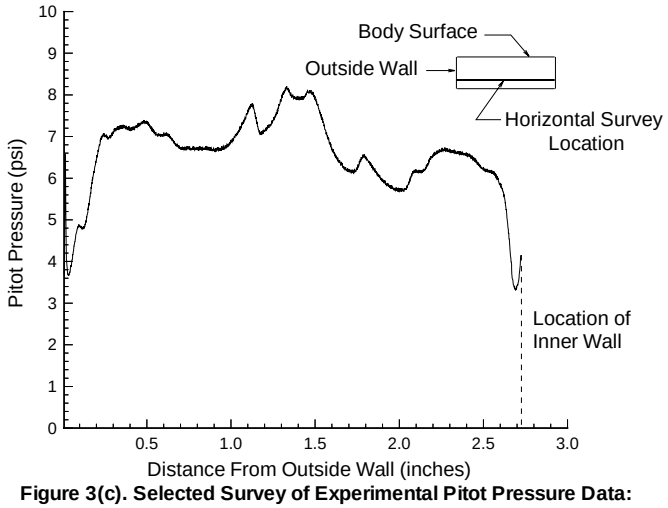

Figure 3(c). Selected Survey of Experimental Pitot Pressure Data: Exit Plane Horizontal Survey.

surveys of pitot pressures at the entrance plane. Figure 3(b) shows a similar survey at the exit plane. Figure 3(c) shows a horizontal survey of pitot pressures at the exit plane. The pitot and static pressure data were used for comparisons with CFD solutions and to obtain experimental internal drag force values. The static pressure data were used only in the internal drag force computations and the calculation of inflow boundary conditions for solution initialization.

III. Computational Analysis

The computational analysis consisted of obtaining CFD solutions, both 2D and 3D, using the Euler and PNS equations. The Euler equations provide inviscid comparisons and take significantly less CPU time to obtain than the viscous solutions. The PNS equations are obtained by eliminating the streamwise diffusion terms from the Navier-Stokes equations. These equations are valid for supersonic, high-Reynolds-number flows that have no streamwise separation[1].

All CFD solutions were obtained using the General Aerodynamic Simulation Program (GASP). GASP is capable of solving the full Reynolds-averaged Navier-Stokes (RANS) equations as well as subsets of those equations, including the thin-layer Navier-Stokes (TLNS), PNS, and Euler equations[5]. The program is a finite volume code which utilizes the upwind/relaxation algorithms. This approach is appropriate for supersonic flows because it correctly represents the physical aspects of the flow by not using any downstream information in the calculation. Additionally, previous research has shown the algorithms to be better at capturing strong shock waves in the supersonic or hypersonic environment[6].

2D Procedure

The computational domain for the 2D solutions is indicated by the shaded region in the bottom view of Figure 1. Only the spanwise and streamwise directions are considered in these solutions. Therefore, the expansion on the upper surface of the inlet module is not represented. Convergence was achieved by specifying a reduction of three orders of magnitude in the residual at each solution plane. A comparison of the computational grids used for the 2D Euler and PNS solutions is shown in Figure 4. The grid shown for the Euler solution has 80 points in both the streamwise and spanwise (I and J) directions, while the PNS grid has 160 points in both directions. The appropriate number of grid points was determined by examining solutions obtained with various grid sizes. It is desirable to use a grid for which the parameters of interest do not change significantly when

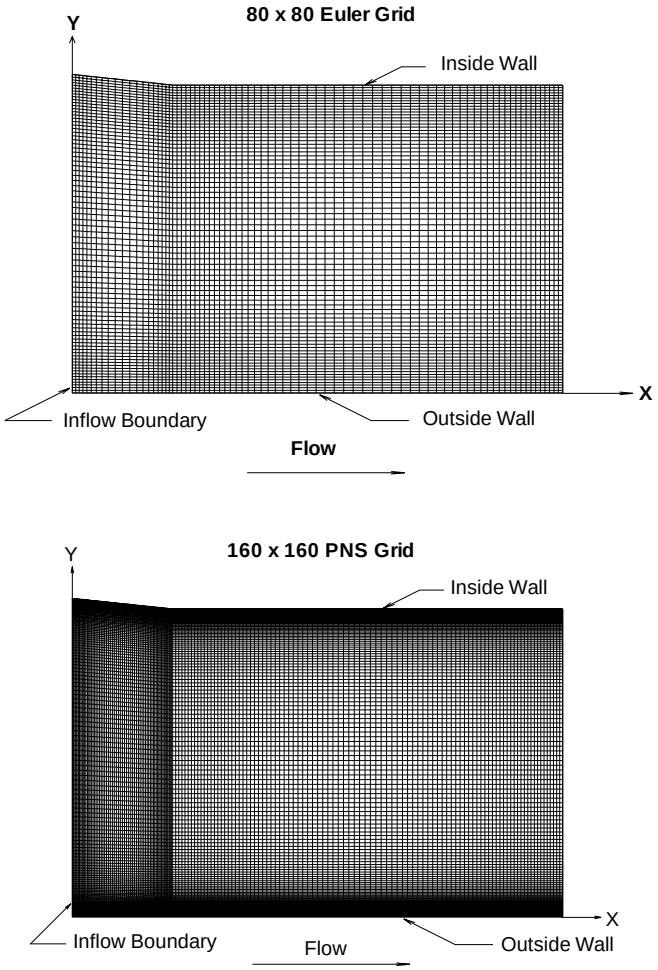

Figure 4. Computational Grids for Two-Dimensional Solutions

additional grid points are added.[7] In order to model the boundary layer growth along the solid boundaries, the viscous grid points are clustered near the inside and outside walls. The amount of clustering necessary is determined by examining the inner law variable, y^+, in each cell center next to the solid boundaries. This variable is defined as[8]

$$y^+ = \sqrt{\frac{\rho_1 U_1 L_1}{\mu_1}} \qquad (1)$$

Prior research indicates that y^+ values less than $\sqrt{2}$ will yield an adequate solution[3]. Both the Euler and PNS solutions were initialized using the experimental pressure data at the entrance plane boundary. Roe's flux difference scheme was used in the crossflow plane; a min-mod flux limiting scheme was used to restrict higher order terms in the crossflow plane; and an implicit LU decomposition scheme was used for time integration[5]. A

tangency boundary condition was imposed on solid walls for the Euler solutions, while a no-slip boundary condition with a fixed wall temperature of 90 degrees Fahrenheit was imposed for PNS solutions. Additionally, the Vigneron technique was utilized in PNS solutions to eliminate the streamwise pressure gradients in subsonic portions of the boundary layer, which prevents the solution from diverging[9].

3D Procedure

The computational domain for 3D solutions is indicated by the oblique view in Figure 1. A reduction of three orders of magnitude in the residual was specified for Euler solutions, while a reduction of four orders of magnitude was used for PNS solutions. Additionally, the PNS solutions were converged to five orders of magnitude on the first five planes of the solution to ensure a good starting solution. The grid used for Euler solutions has 80 points in the I and J directions and 40 points in the vertical (K) direction. The PNS solutions were obtained using a grid with 160 points in the I and J directions, with 80 points in the K direction. The inflow boundary conditions were specified using two methods available in the code: a constant boundary and a variable boundary. The constant boundary method initializes each cell center at the entrance plane with uniform flow-field properties. The variable boundary method inputs a distribution of flow-field properties across the entrance plane. In other words, this method requires the specification of flow-field properties (pressure, density, temperature, and three velocity components) for each individual cell center at the entrance plane. The flow-field properties are calculated from experimental static and pitot pressure data. This approach accurately models the forebody boundary layer growth at the entrance plane as well as inclusion of flow angularity. The effect of varying the local flow angles at the inflow boundary is examined by prescribing different angle values using the variable boundary method. Specifically, the effects of zero flow angularity, variable flow angularity, and a constant downward flow angle across the entrance plane are examined individually in this paper. Several changes were made from the 2D computational procedure to obtain the 3D solutions. These include the use of Van Leer's flux vector splitting in the crossflow plane, a Van Albeda-type smooth limiter to restrict higher order terms, and the use of an approximate factorization scheme for time integration[5]. The CFL number specified was also observed to have an effect on the solution. GASP computes local time steps at each solution plane based on the CFL number specified[5]. As the grid size increased, it was necessary to lower the CFL number to obtain a well-converged solution. However, a decrease in CFL number resulted in an increase in CPU time, so it was advantageous to use the largest value of the CFL number that would allow the code to run.

Results and Discussion

The computational solutions were compared with the pitot pressure surveys taken at the exit plane of the inlet. The 2D Euler and PNS solutions were examined first followed by 3D Euler and PNS Solutions. Comparisons of various 3D PNS solutions were examined to show the effects of computational parameters on exit plane pitot pressure distributions. These parameters included residual convergence tolerance, size of the computational grid and the method of prescribing the inflow boundary conditions.

A comparison of 2D Euler and PNS solutions with the horizontal exit plane experimental pitot pressure survey is shown in Figure 5. The Euler solution took

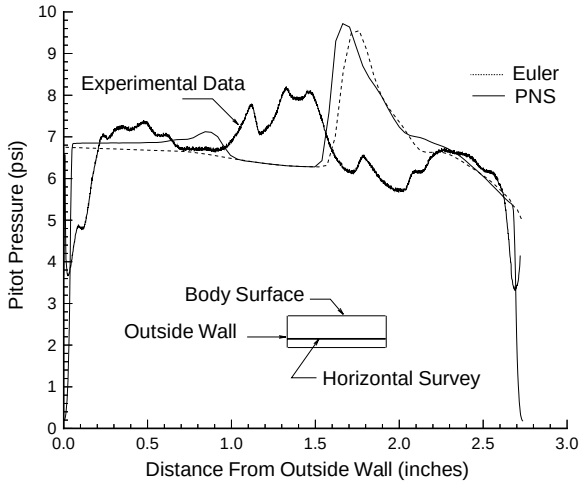

Figure 5. Computational Exit Plane Pitot Pressure Surveys: Two-Dimensional Euler and PNS Solutions

approximately 70 seconds of CPU time to obtain on NASA Langley's CRAY-2 computer, whereas the PNS solution took approximately 47 minutes. The sharp rise in pitot pressure values shown in both CFD solutions indicates a shock wave caused by the compression along the inside wall. The computational data shows a local over-prediction of pitot pressure values at the location of this disturbance. This is expected since the upper surface expansion is not taken into account. Its location is also incorrectly predicted when compared to the experimental data. The PNS solution indicates a weaker, oblique shock wave, caused by formation of the boundary layer along the outside wall, at a location approximately 0.85 inches from the outside wall. The location of this disturbance is also not correctly predicted. The PNS solution also predicts the boundary layer along the solid walls, as

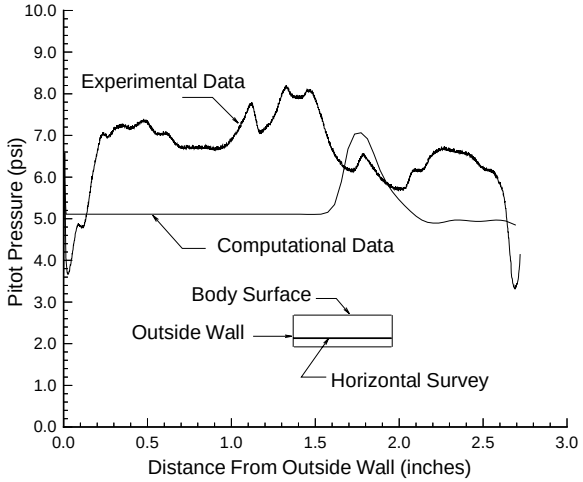

Figure 6. Computational Exit Plane Pitot Pressure Survey: Three-Dimensional Euler Solution

indicated by the sharp drop in pitot pressure values. However, the extent of the boundary layer next to the outside wall is underpredicted. The results of a 3D Euler solution is shown in Figure 6. The CFD data shown in this figure are for a horizontal survey at the approximate location of the experimental pitot pressure survey at the exit plane. The solution shown took approximately 150 seconds to obtain on NASA Langley's CRAY-2 computer. The pressure values at the exit plane are significantly lower than experimental values across the exit plane. The location of the shock wave caused by the compression on the inside wall is also incorrectly predicted. None of the Euler solutions obtained provided good comparisons with the experimental pressure data. This leads to the conclusion that the viscous effects within the flow field are too dominate for an inviscid solution to provide any reasonable predictions of the internal inlet flow field.

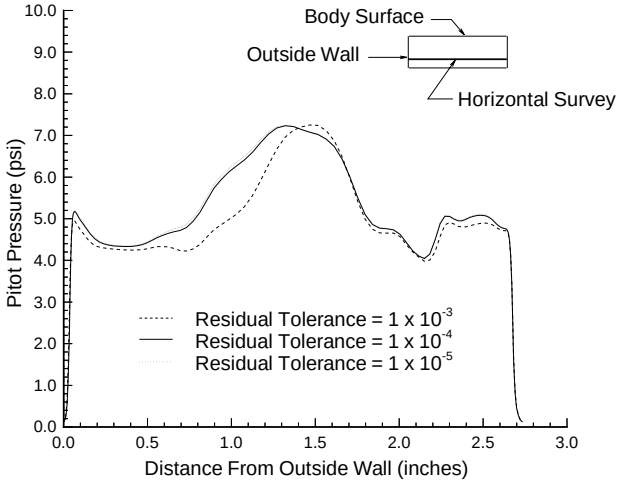

Figure 7. Effect of Residual Tolerance on Three-Dimensional PNS Solutions: Exit Plane Pitot Pressure Surveys

The 3D PNS solutions were examined to show the effects of various computational parameters on solution accuracy. The effect of the residual convergence tolerance is shown in Figure 7. The solutions shown were obtained using a variable inflow boundary with variable flow angularity in the vertical direction. The grid used had 120 points in the I direction, 140 points in the J direction and 80 points in the K direction. The smaller grid size was used for the tolerance study to reduce memory storage requirements. Solutions were obtained using a three, four, and five orders of magnitude reduction in the residual at each solution plane. There is essentially no variation in the solutions obtained with four and five orders of magnitude reduction, while there is a significant variation in the solutions obtained with three and four orders of magnitude reduction. This indicates that a four orders of magnitude reduction in the residual is appropriate and therefore was used in subsequent CFD solutions.

A second parameter which affects solution accuracy is the size of the computational grid. Increasing the number of grid points in each direction has an effect on the exit plane pitot pressure distribution. Figure 8 shows the effect of varying the number of grid points in the I, J, and K directions on exit plane pitot pressure values. The grid sizes are indicated as the number of points

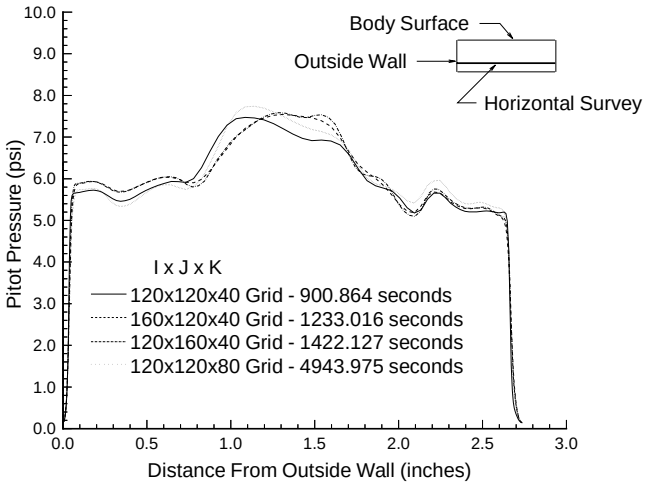

Figure 8. Effect of Grid Size on Three-Dimensional PNS Solutions: Exit Plane Pitot Pressure Surveys

in the I x J x K directions. The figure shows a variation in the exit plane pitot pressure distribution when grid points are added in each direction, up to 160 in the I and J directions and 80 in the K direction. This indicates that the minimum number of grid points required for an adequate solution is 160 in the I and J directions and 80 in the K direction. The CPU times indicated for each solution are for NASA Langley's CRAY-2 computer. It should also be noted that these grid sizes require a large

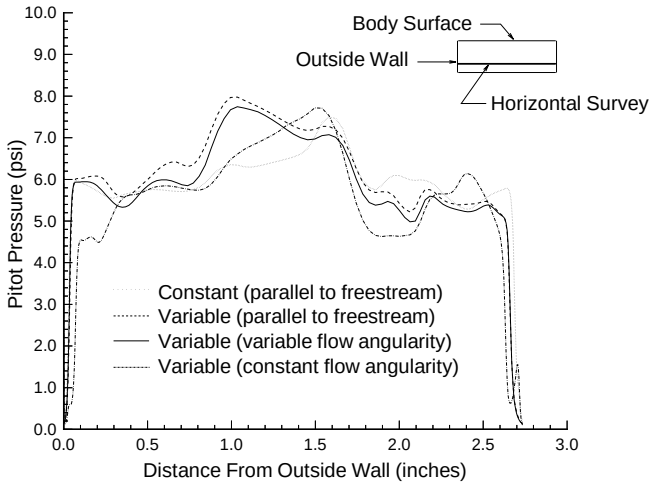

Figure 9. Effect of Inflow Boundary Conditions on Three-Dimensional PNS Solutions: Exit Plane Pitot Pressure Surveys

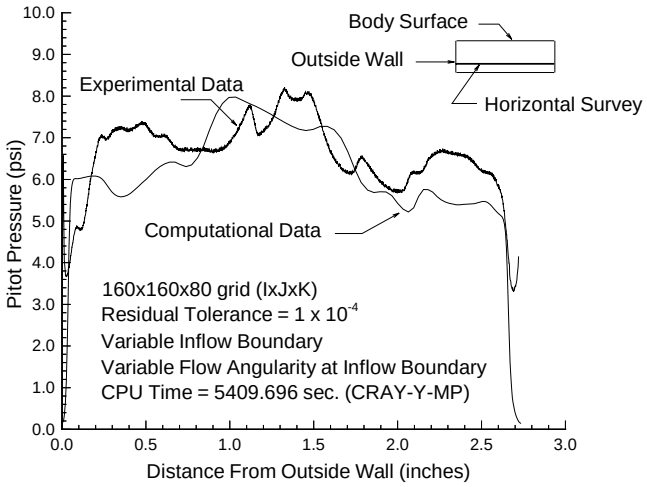

Figure 10. Computational Exit Plane Pitot Pressure Survey: Three-Dimensional PNS Solution

amount of memory storage, up to 60 million words for the largest grids used.

The third computational parameter examined is the method of prescribing the inflow boundary conditions for solution initialization. Figure 9 shows the effect of inflow boundary conditions on the exit plane pitot pressure values. The effect of using the constant boundary description and the variable boundary description is shown. Also, The effect of varying the local flow angles is shown. It is necessary to use the variable boundary description in order to accurately model the forebody boundary layer growth as well as the inclusion of flow angularity at the entrance plane. Figure 9 shows a significant variation between the exit plane pitot pressure distributions for the constant and variable boundary methods. There is a slight variation in the exit plane pitot pressure values when the flow angles are allowed to vary in the vertical direction.

The PNS solutions showed the best comparisons with the experimental data. Figures 10 and 11 show data for a solution which was obtained using a grid with 160 points in the I and J directions and 80 points in the K direction. The solution was initialized with a variable inflow boundary and variable flow angularity in the vertical direction. Based on experimental data comparisons, this appears to be the most accurate solution that was obtained. Figure 10 shows comparisons between computational data and experimental data for a horizontal exit plane pitot pressure survey. The agreement between the data is generally good, although some discrepancies still exist. The CFD data shows a local underprediction of pressure values near the inside and outside walls. Additionally, the solution shows an underprediction of the size of the boundary layer. Figures 11(a) through

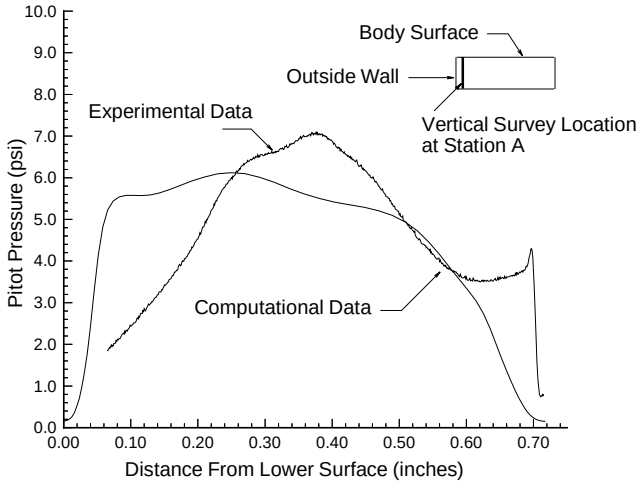

Figure 11(a). Exit Plane Pitot Pressure Vertical Survey at Station A

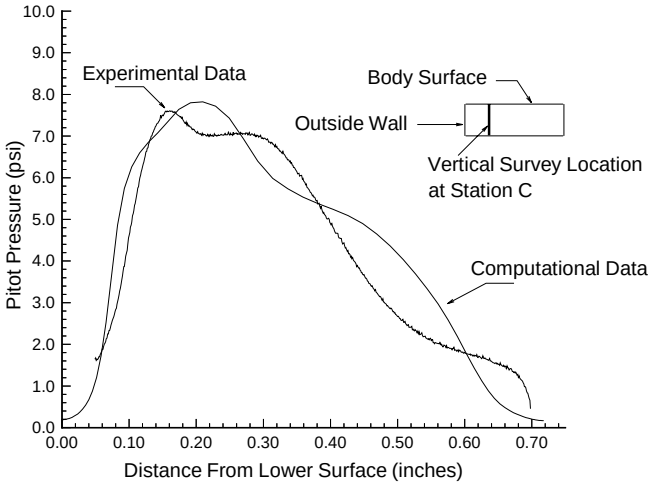

Figure 11(b). Exit Plane Pitot Pressure Vertical Survey at Station C

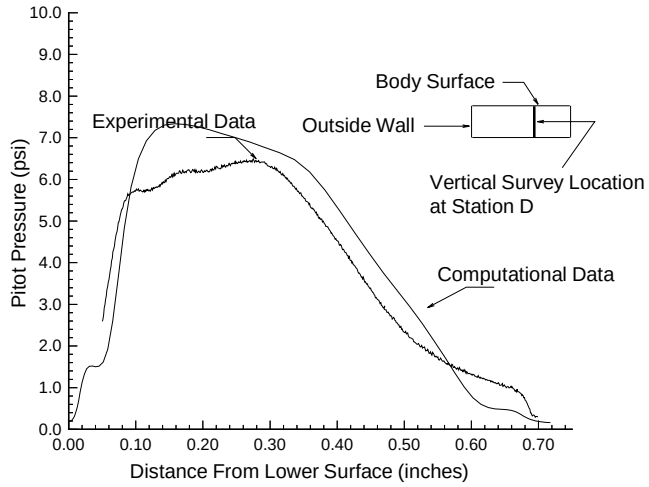

Figure 11(c). Exit Plane Pitot Pressure vertical Survey at Station D

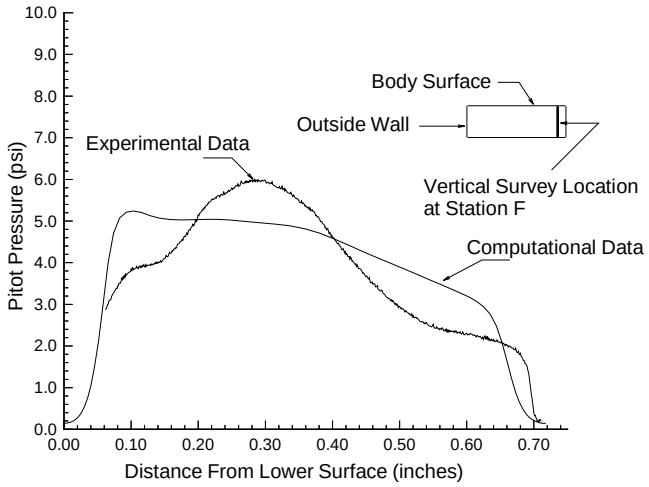

Figure 11(d). Exit Plane Pitot Pressure Vertical Survey at Station F

11(d) show comparisons between computational data and vertical pitot pressure surveys at the exit plane. The agreement at stations C and D appears to be better than that at the stations closest to the solid walls.

IV. Internal Inlet Drag Analysis

Due to the difficulties associated with experimentally measuring the internal inlet drag, it is desirable to use inlet CFD solutions to estimate this value. A method for estimating the internal inlet drag using CFD data is outlined in the following section. Predictions for the internal drag force using 3D PNS solutions are given. The sensitivity of CFD drag predictions to computational parameters is examined in order to indicate the level of complexity of the computational procedure required to obtain an adequate internal drag estimate. An assessment of experimental and computational drag estimation methods is made.

Procedure

The internal inlet drag calculations are made using the momentum equation to calculate the momentum loss through the inlet control volume. This equation can be used to obtain an expression for the internal drag force as a function of pressure forces and momentum fluxes at the entrance and exit planes. The individual components of this expression can be computed using either computational or experimental data.

The integral form of the momentum equation may be written as[10]

$$\vec{\vec{F}} = \vec{\vec{F}}_S + \vec{\vec{F}}_B = \frac{\partial}{\partial t}\iiint_{CV} \vec{\vec{V}}\rho dV + \iint_{CS} \vec{\vec{V}}\rho\vec{\vec{V}}d\vec{\vec{A}} \quad (2)$$

where,

$\vec{\vec{F}}$ = Net force acting on the control volume,
$\vec{\vec{F}}_S$ = Surface forces on the control volume,
$\vec{\vec{F}}_B$ = Body forces on the control volume,

$$\frac{\partial}{\partial t}\iiint_{CV} \vec{\vec{V}}\rho dV = \text{Rate of change of momentum,}$$

and

$$\iint_{CS} \vec{\vec{V}}\rho\vec{\vec{V}}d\vec{\vec{A}} = \text{momentum flux.}$$

The surface forces consists of a shear force on the control volume and pressure forces.

$$\vec{\vec{F}}_s = R_x + \left(\int_1 p_1 dA_1 - \int_2 p_2 dA_2\right) \quad (3)$$

Assuming steady flow and no body forces acting on the control volume and rewriting the streamwise component of the momentum equation yields

$$R_x + \int_1 p_1 dA_1 - \int_2 p_2 dA_2 = \dot{m}_2 u_2 - \dot{m}_1 u_1 \quad (4)$$

where the subscript 1 represents the entrance plane and the subscript 2 represents the exit plane. Since the internal part of the body is contained within the control volume, there is another force acting on the body that is equal and opposite to the shear force acting on the control volume:

$$F_I = -R_x \quad (5)$$

By substitution in to Equation 4 and solving for the internal force, an equation for the internal force as a function of pressure forces and momentum fluxes is obtained, as follows:

$$F_I = \int_1 p_1 dA_1 - \int_2 p_2 dA_2 - (\dot{m}_2 u_2 - \dot{m}_1 u_1) \qquad (6)$$

The internal force is calculated using Equation 6 from pitot pressure and static pressure data. Both computational and experimental data can be used. These data can be used to calculate the individual terms in the equation using the following procedure, which is based on one-dimensional gas dynamics. The local Mach number is computed iteratively based on the Rayleigh-Pitot formula[11]:

$$\frac{P_p}{P} = \left(\frac{(\gamma+1)M^2}{(2)}\right)^{\frac{\gamma}{(\gamma-1)}} \left(\frac{\gamma+1}{2\gamma M^2 - (\gamma-1)}\right)^{\frac{1}{(\gamma-1)}} \qquad (7)$$

The static temperature is calculated based on a known freestream total temperature and the Mach number computed in Equation 7:

$$T = T_o \left(1 + \frac{\gamma-1}{2} M^2\right)^{-1} \qquad (8)$$

The total pressure is calculated based on the static pressure and Mach number:

$$P_o = P \left(1 + \frac{\gamma-1}{2} M^2\right)^{\frac{\gamma}{\gamma-1}} \qquad (9)$$

The static temperature and Mach number are also used to compute the total velocity:

$$V = M\sqrt{\gamma R T} \qquad (10)$$

The streamwise component of velocity, u, can be determined from the local flow angle and total velocity. The mass flow rate per unit area is then calculated based on total pressure, total temperature, and Mach number:

$$\frac{\dot{m}}{\Delta A} = \frac{P_o}{\sqrt{T_o}} \sqrt{\frac{\gamma}{R}} \frac{M}{\left(1 + \frac{\gamma-1}{2} M^2\right)^{\frac{\gamma+1}{2(\gamma-1)}}} \qquad (11)$$

The components of equation (6) can be then be computed using the following expressions, used to sum the contributions of momentum and pressure force terms at the individual data locations:

$$(\dot{m}V) = \sum_j \sum_k \left(\frac{\dot{m}}{\Delta A}\right)_{(j,k)} (\Delta Y_j)\,(\Delta Z_k)\,(u_{j,k}) \qquad (12)$$

and

$$\int p dA = \sum_j \sum_k p_{(j,k)}\,(\Delta Y_j)\,(\Delta Z_k) \qquad (13)$$

The above steps are repeated for the entrance and exit planes of the inlet in order to evaluate the internal force.

Results and Discussion

Internal drag force computations were made using experimental pressure data as well as 3D Euler and PNS solutions. The Euler solutions did not yield any reasonable values for internal drag force and therefore are not presented here. The drag force values obtained using the PNS solutions were highly sensitive to the computational procedure used. Specifically, the residual convergence tolerance, the grid size, and inflow boundary conditions used had a significant effect on the drag force value.

Table 1 shows internal drag force computations based on 3D PNS solutions. The residual tolerance criterion has only a slight effect on the internal drag force. There is a difference of 0.006 lbf between the values obtained using three and four orders of magnitude reductions in the residual at each solution plane. There is no difference between the values obtained using four and five orders of magnitude reductions. This is a further indication that a four orders of magnitude reduction in the residual is appropriate.

The effect of varying the number of grid points in each direction is shown by comparisons of solutions obtained with different grid sizes. These results indicate that the internal drag force value is highly sensitive to the size of the grid used. An increase in the number of grid points in the vertical direction results in an decrease in the drag force, while increasing the number of points in the streamwise and spanwise directions results in an increase in drag force, if the number of points in the other directions are held constant. There is only a slight difference between the value obtained with a 120 x 140 x 80 grid and the value obtained with a 160 x 160 x 80 grid.

The results also indicate that the computed force values are highly sensitive to the method of prescribing the inflow boundary conditions for solution ini-

Table 1. Sensitivity of Drag Predictions to CFD Input Parameters

GRID SENSITIVITY

Grid Size	Internal Force (lbf)
120x120x40	0.044
120x120x80	0.032
120x160x40	0.059
160x120x40	0.065
120x140x80	0.035
160x160x80	0.038

Variable Inflow Boundary, Inflow velocities parallel to freestream, 3 orders of magnitude residual reduction.

BOUNDARY CONDITIONS

Condition	Internal Force (lbf)
Constant Velocities Parallel to Freestream	0.054
Variable Velocities	
Parallel Velocities	0.038
Variable Flow Angularity	0.037

160x160x80 Grid, 4 Orders of magnitude reduction in residual.

RESIDUAL TOLERANCE

Reduction	Internal Force (lbf)
3 Orders	0.053
4 Orders	0.047
5 Orders	0.047

120x140x80 Grid, Variable flow angularity at entrance plane.

tialization. The effect of using a variable boundary rather than constant flow field properties at the entrance plane is shown. The drag force is also affected by adjusting the flow angularity in the vertical direction. These results suggest that it is necessary to resolve the flow field properties and local flow angles to a high degree of certainty before CFD predictions for internal drag force can be considered accurate.

The accuracy of the CFD predictions is difficult to assess. The solution shown in figures 10 and 11 is the most accurate one that was obtained, in terms of exit plane pitot pressure comparisons. This solution yields a drag force values of 0.037 lbf. However, there are still some discrepancies between the CFD and experimental pitot pressure values at the inlet exit plane. These uncertainties are most likely the result of an inadequate amount of experimental data to initialize the solution. It is difficult to calculate the flow field properties at the inflow boundary from the limited number of surveys available It is impossible to make an accurate determination of the local flow angles at the entrance plane from existing experimental data. These results suggest that more accurate CFD predictions may be obtained by initializing the inlet solution with a forebody CFD solution. The CFD analysis indicates that the internal inlet drag accounts for 1.51 percent of the experimentally measured balance force of 4.886 lbf.

The experimental data analysis suggests that the limited number of probe surveys available are not sufficient to provide an accurate accounting of the internal inlet drag. When the procedure previously described is followed using the experimental pressure data, an internal force value of -0.40 lbf is obtained. A negative value suggests that a net thrust is produced. This is obviously unrealistic since a thrust component would not be produced by flow through an inlet. The unrealistic value is most likely due to the fact that the limited number of probe surveys are unable to capture the complex flow structure of the inlet. Additionally, since the probe is not sensitive to flow angularity, the streamwise component of velocity cannot be determined for use in Equation 12. Therefore, three-dimensional momentum effects are not included in the internal drag estimate. Furthermore, the quality of the static pressure data is questionable, since each survey had pressure variations that approached the actual pressure value along the profile. Finally, at the freestream Reynolds numbers which flow-field pressures were taken, the boundary layer along the body (upper) surface may have transitioned or become fully turbulent. No attempt was made to determine the nature of the boundary layer inside the inlet module. The results suggest that it is necessary to develop an alternative method

of experimentally determining the internal inlet drag force.

V. Conclusions

A computational analysis and an internal inlet drag analysis were performed for a single inlet module of a generic, body-mounted scramjet propulsion system. The purpose of the study was to assess the feasibility of obtaining predictions for the internal drag force on the inlet region using computational methods. The computational procedure consisted of obtaining 2D and 3D inviscid and viscous CFD solutions on the inlet flow field. The 3D PNS solutions were used to obtain internal drag force predictions, which were compared to those obtained from experimental pressure data.

The CFD analysis indicates that the 3D PNS solutions generally show good agreement with exit plane pitot pressure values. The difficulty in obtaining accurate solutions focuses on the determination of the appropriate grid size and the method of prescribing inflow boundary conditions. The entrance plane boundary conditions are difficult to resolve from experimental data alone and a forebody CFD solution is needed to accurately compute the local flow angles at the inflow boundary.

The internal inlet drag analysis indicates that the internal drag values obtained from CFD solutions are highly sensitive to the grid size and method of solution initialization. Additionally, it is difficult to assess the accuracy of CFD drag predictions due to discrepancies between the CFD and experimental pressure values at the inlet exit plane. These discrepancies are most likely the result of an insufficient amount of data to accurately compute the flow field properties and local flow angles at the inflow boundary. These results suggest that a forebody CFD solution may be required to initialize the inlet flow field. The experimental data analysis yields an unrealistic value for the internal inlet drag, suggesting that the amount of data obtained is insufficient to accurately capture the complex flow structure of the inlet and to make an accurate estimation of the internal drag.

References

[1]Dwoyer, Douglas L. and Kumar, Ajay. "Computational Analysis of Hypersonic Airbreathing Aircraft Flow Fields," AIAA Paper 87-0279, January 1987.

[2]McClinton, Charles R.; Bittner, Robert D., and Kamath, Pradeep S. "CFD Support of NASP Design," AIAA Paper 90-5249, October 1990.

[3]Huebner, Lawrence D.; Pittman, James L, and Dilley, Arthur D. "Hypersonic Parabolized Navier-Stokes Code Validation on a Sharp-Nosed Cone," *Journal of Aircraft*, Volume 26, Number 7, July 1989, pp.650-656.

[4]Mehta, Unmeel B. "The Aerospace Plane Design Challenge: Credible Computational Fluid Dynamics Results," AIAA Paper 90-5248, October 1990.

[5]Walters, Robert W.; Slack, David C.; Cinnella, Pasquale; Applebaum, Michael; and Frost, Corey. *A User's Guide to GASP*, Virginia Polytechnic Institute and State University, November 1990.

[6]Newsome, Richard W.; Walters, Robert W.; Thomas, James L. "An Efficient Iteration Strategy for Upwind/Relaxation Solutions to the Thin-Layer Navier-Stokes Equations," AIAA Paper 87-1113, June 1987.

[7]Finley, Dennis B. "Hypersonic Aerodynamics Considerations and Challenges," AIAA Paper 90-5222, October 1990.

[8]Richardson, Pamela F. and Parlette, Edward B. "Comparison Between Experimental and Numerical Results for a Research Hypersonic Aircraft," *Journal of Aircraft*, Volume 27, Number 4, April 1990, pp.300-305

[9]Vigneron, Yvon C.; Rakich, John V.; Tannehill, John C. "Calculation of Supersonic Viscous Flow Over Delta Wings with Sharp Subsonic Leading Edges," AIAA Paper 78-1137, July 1978.

[10]Bertin, John J. and Smith, Michael L. *Aerodynamics For Engineers*. Englewood Cliffs, NJ: Prentice Hall, 1989.

[11]Anderson, John D. *Fundamentals of Aerodynamics*. New York: McGraw Hill, 1984.